nature portfolio

https://doi.org/10.1038/s41586-026-10869-x

Supplementary information

Perovskite–organic tandem solar cells with a photo-transformable stabilizer

In the format provided by the authors and unedited

Supplementary Information

Perovskite–organic tandem solar cells with a photo-transformable stabilizer

Ruihan Wu[1,2], Shucheng Qin[1], Tianwei Zou[1,2], Xin Jiang[1,2], Senyao Wang[1,2], Siyu Zhuang[1,2], Hongyu Li[3], Yiyang Wang[1,2], Siguang Li[1,2], Minchao Liu[1,2], Yishun Feng[1,2], Yufei Gong[1,2], Haozhe He[1,2], Peiwen Liao[1,2], Yu Chen[4], Jinyuan Zhang[1], Xiaojun Li[1], Lei Meng[1,2], Yongfang Li[1,2,5*]*

[1] *Beijing National Laboratory for Molecular Sciences, CAS Key Laboratory of Organic Solids, Institute of Chemistry, Chinese Academy of Sciences, Beijing 100190, China*

[2] *School of Chemical Science, University of Chinese Academy of Sciences, Beijing 100049, China*

[3] *East China University of Science and Technology, Shanghai 200237, China*

[4] *Beijing Synchrotron Radiation Laboratory, Institute of High Energy Physics, Chinese Academy of Sciences, Beijing, 100049, China*

[5] *Laboratory of Advanced Optoelectronic Materials, Suzhou Key Laboratory of Novel Semiconductor Materials and Devices, College of Chemistry, Chemical Engineering and Materials Science, Soochow University, Suzhou, Jiangsu 215123, China*

***Corresponding authors. E-mail:** menglei@iccas.ac.cn (L. Meng); liyf@iccas.ac.cn (Y. Li)

Table of Contents

Supplementary Figures

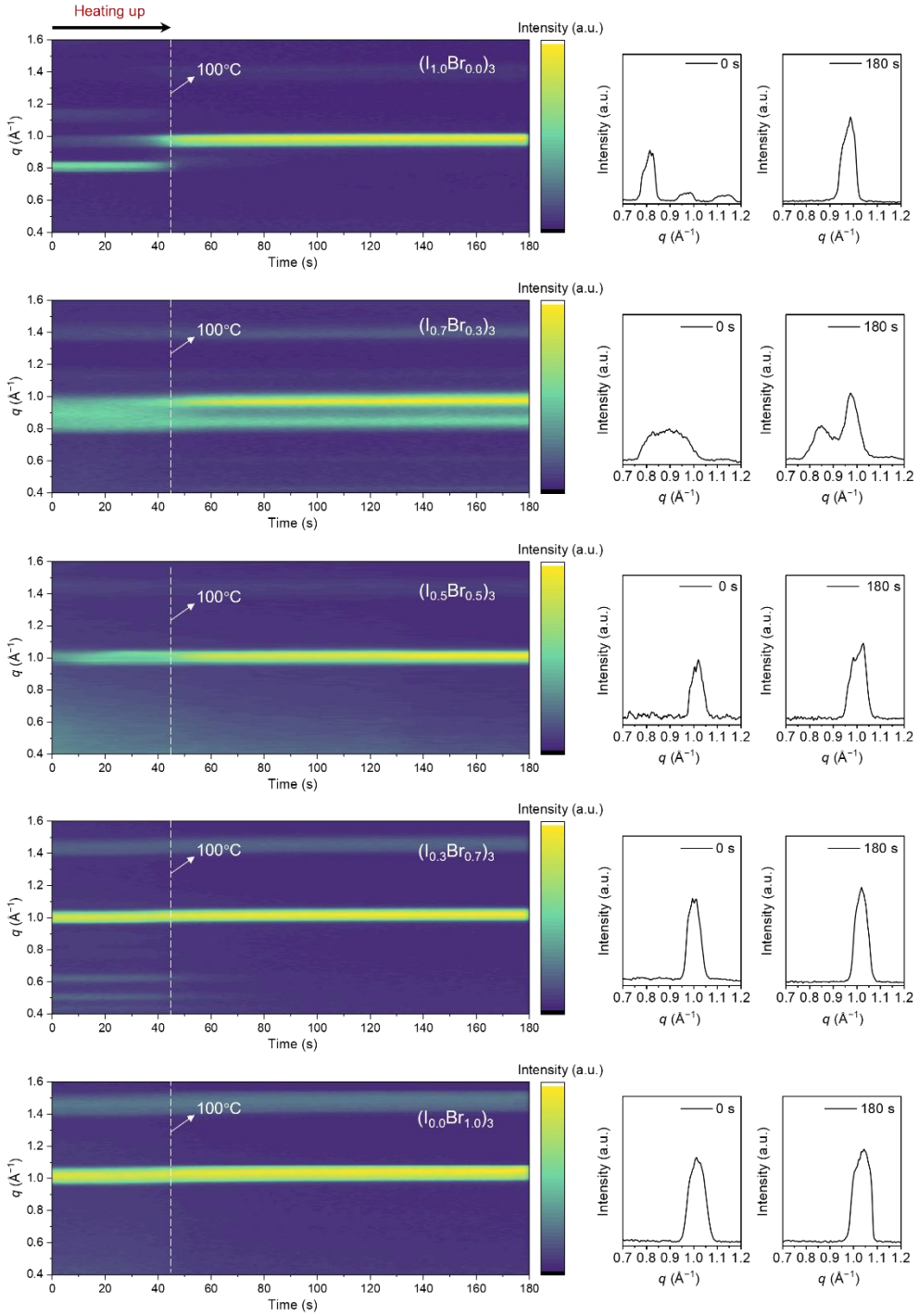

Supplementary Figure 1. Crystallization behavior of $FAPb(I_{1-x}Br_x)_3$ perovskite films with increasing Br content (20 mol% MACl was added to assist crystallization) during

annealing. The left panels present the time-resolved grazing-incidence wide-angle X-ray scattering (GIWAXS) intensity maps and the dashed lines indicate the time point at which the substrate temperature reached 100 °C (heating was initiated at 0 s from an initial substrate temperature of 25 °C). The right panels show the corresponding one-dimensional GIWAXS profiles extracted from the time-resolved maps at 0 and 180 s, representing the initial and final crystallization characteristics. Unlike MA-based perovskites, FA-based perovskite compositions do not exhibit a pronounced $MA_2Pb_3I_8 \cdot 2DMSO$ diffraction peak after antisolvent dripping in the wet-film state. $FAPbI_3$ wet films exhibited the δ phase after antisolvent quenching, which gradually converted into the α phase during annealing. With increasing Br content, the perovskite α phase formed directly in the initial wet-film state, bypassing the δ-phase intermediate. Specifically, the high-Br WBG perovskite with 50 mol% Br exhibited phase separation in both the initial wet film at 0 s and the final annealed film at 180 s.

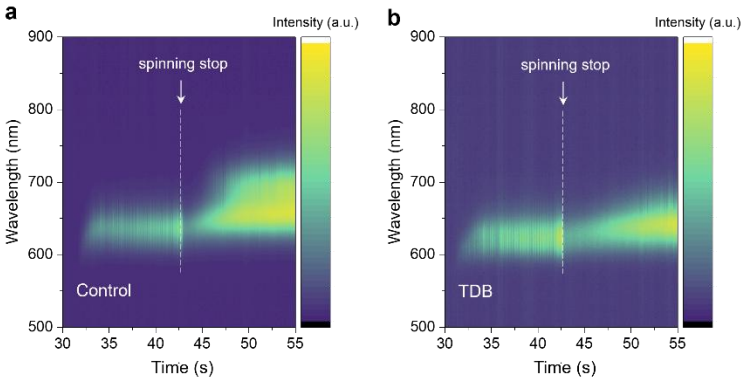

Supplementary Figure 2. *In situ* steady-state photoluminescence (PL) characterization of phase evolution in control and TDB-treated WBG perovskite films during spin-coating.

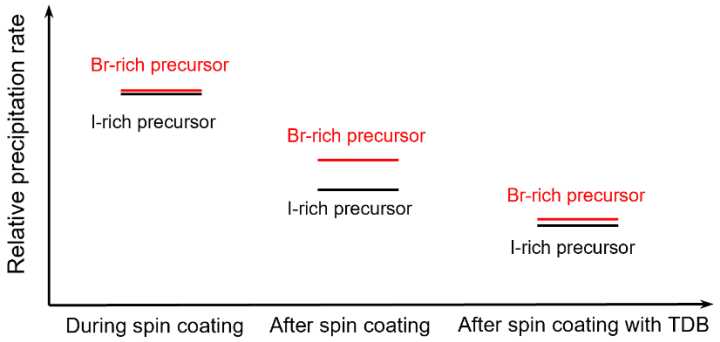

Supplementary Figure 3. Schematic illustration of the precipitation behavior of Br-rich and I-rich precursors during spin-coating. The dissolution of Br-rich and I-rich precursors is governed by their different coordination interactions with DMF and DMSO solvent molecules[1]. During spin-coating, the rapid evaporation of solvent molecules drives the simultaneous precipitation of both precursors, thereby diminishing the influence of their intrinsic solubility disparity. Once spin-coating stops, solvent evaporation slows substantially, allowing the solubility difference between the two precursor species to dominate the precipitation kinetics and promote the preferential precipitation of the less soluble Br-rich phase. Upon TDB addition, the interactions between TDB and the precursor species stabilize the solvated precursors and retard their crystallization, thereby suppressing the preferential precipitation of the Br-rich phase.

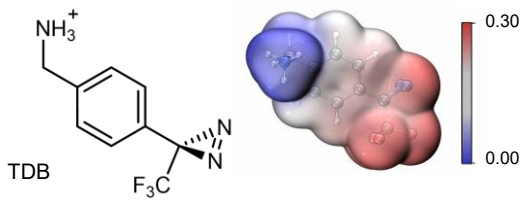

Supplementary Figure 4. Molecular structure and electrostatic potential map of TDB. TDB consists of a benzylammonium moiety with a para-substituted trifluoromethyl-diazirine group. As revealed by the electrostatic potential map, the diazirine moiety exhibits a pronounced electron-rich region owing to the lone-pair electrons on the two nitrogen atoms.

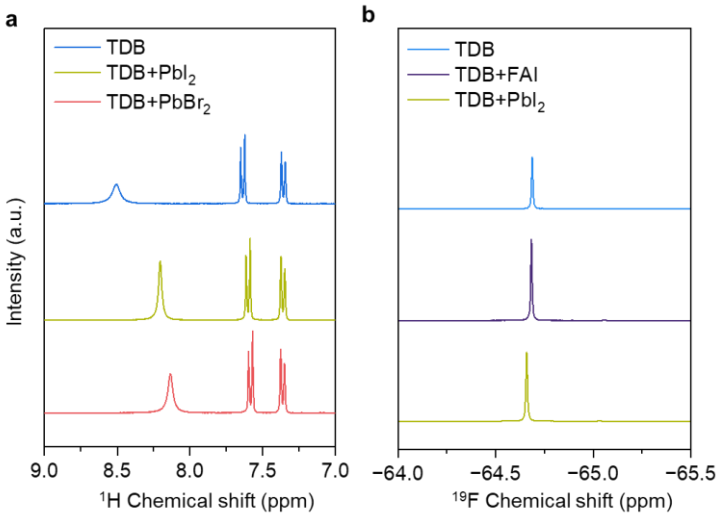

Supplementary Figure 5. **a**, ^{1}H NMR spectra of TDB, TDB+PbI_2, and the TDB+$PbBr_2$ mixture. **b**, ^{19}F NMR spectra of TDB, TDB+FAI, and TDB+PbI_2. Upon addition of PbI_2 or $PbBr_2$, the NH_3^+ proton of TDB shifted upfield, suggesting enhanced local shielding arising from the electrostatic interactions between halide anions and the ammonium group. Meanwhile, the aromatic proton ortho to the trifluoromethyl diazirine group also exhibited an upfield shift. Given that a purely inductive effect transmitted through the diazirine group is unlikely to account for the observed shift over such a distance, we attribute it to anisotropic shielding arising from the π-electron distribution of the diazirine unit[2]. To verify this hypothesis, we performed DFT calculations (Supplementary Fig. 6). DFT results indicate that coordination between Pb cation and TDB reorients the diazirine ring, thereby bringing the ortho aromatic proton into a more shielded region. The ^{19}F NMR spectra of the TDB+FAI and TDB+PbI_2 mixtures showed slight changes, suggesting that the F atoms in the $–CF_3$ group provide weak assisted interactions that cooperatively stabilize the interaction between the diazirine nitrogen atoms and perovskite precursor.

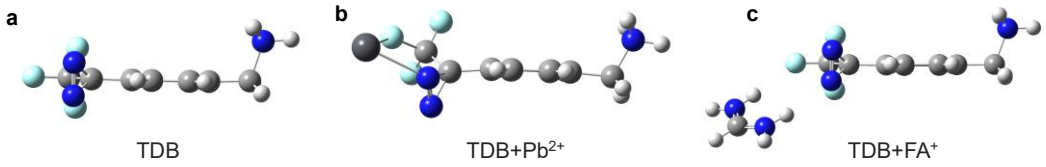

Supplementary Figure 6. **a**, Optimized molecular structure of TDB. **b**, Optimized model of the complex between TDB and Pb^{2+} cation. **c**, Optimized model of the complex between TDB and FA^{+} cation. Carbon atoms are shown as grey spheres, hydrogen as white, nitrogen as blue, fluorine as light cyan, lead as black.

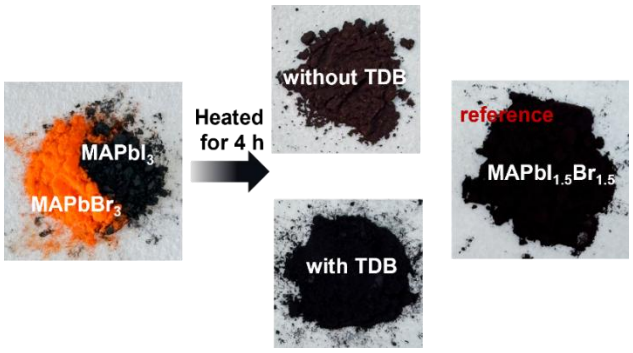

Supplementary Figure 7. Photographs of the powder samples used for ^{207}Pb solid-state NMR characterization showing the changes in $MAPbI_3$ and $MAPbBr_3$ powders without and with TDB after heating in the dark at 80 °C for 4 h.

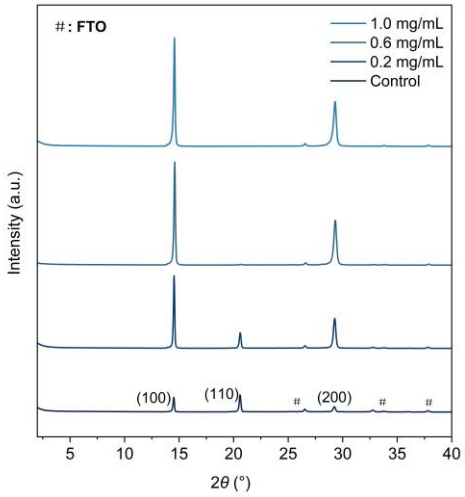

Supplementary Figure 8. X-ray diffraction patterns of the perovskite films treated with different concentrations of TDB.

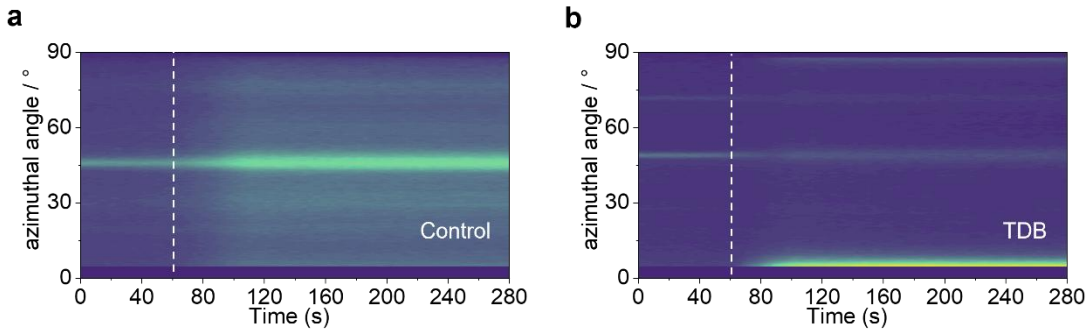

Supplementary Figure 9. Azimuthal angular intensity of the perovskite diffraction signal as a function of time for the control and TDB-treated films during annealing. Both films showed similarly broad angular distributions before heating, but upon annealing, the TDB-treated film exhibited a clear azimuthal redistribution with the scattering intensity concentrated near 0°, whereas the control film remained broadly distributed around 45° (the dashed lines indicate the onset of annealing at 100 °C).

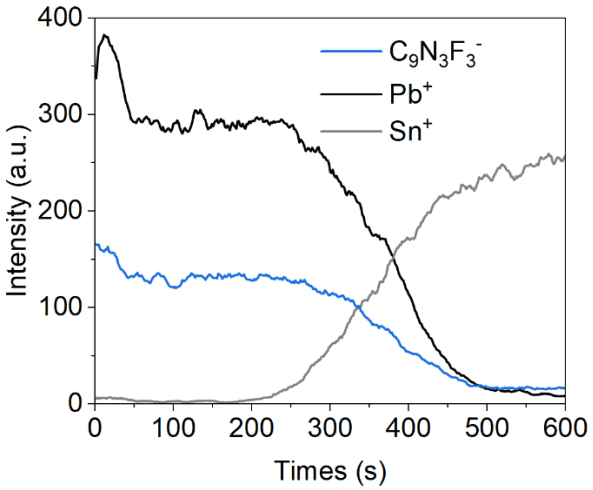

Supplementary Figure 10. The time-of-flight secondary-ion mass spectrometry (ToF-SIMS) depth profile of the target perovskite film. The signal of $C_9N_3F_3^-$ indicates the vertical distribution of TDB.

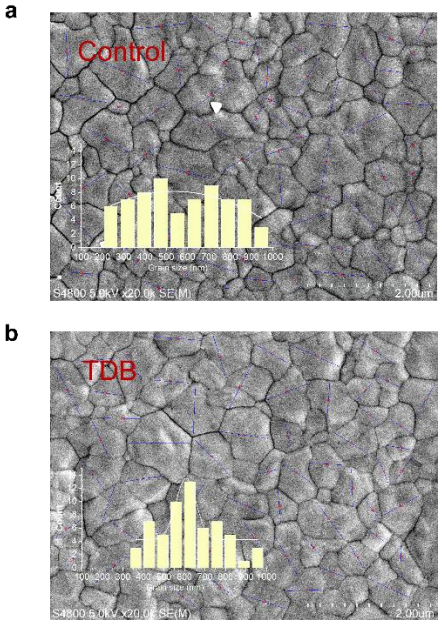

Supplementary Figure 11. Top-view SEM images of the (**a**) control and (**b**) TDB-treated perovskite films. The control film has small average grain sizes and widespread grain boundaries compared with the target film. The insets show the corresponding grain-size distributions extracted from the SEM images.

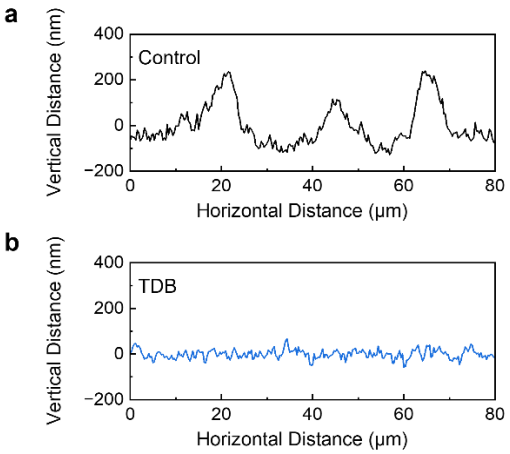

Supplementary Figure 12. Corresponding surface altitude deviation for (**a**) the control film and (**b**) the TDB-treated film.

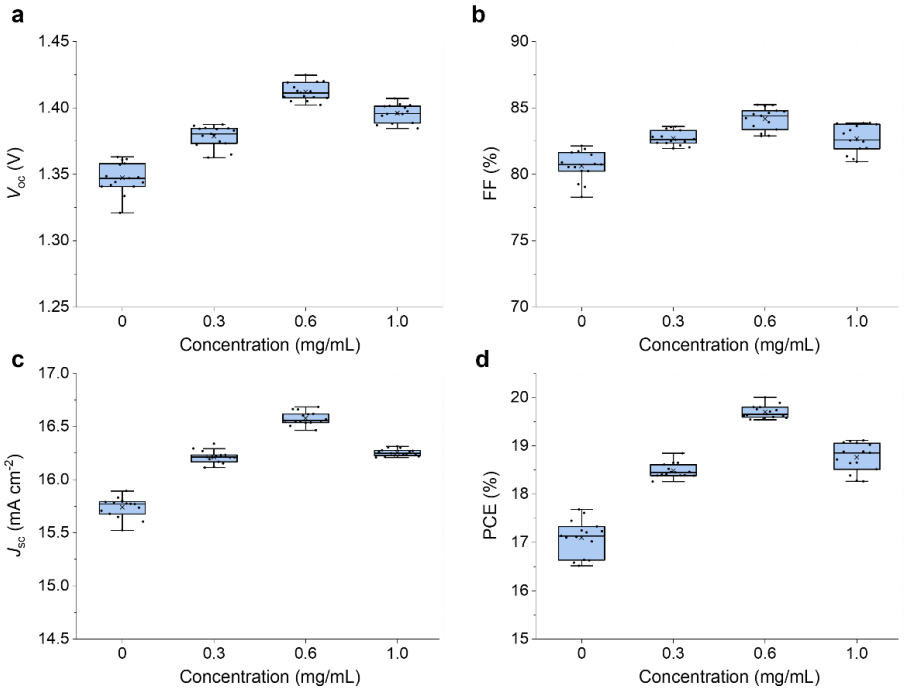

Supplementary Figure 13. Distributions of the (**a**) open-circuit voltage (V_{oc}), (**b**) fill factor (FF), (**c**) short-circuit current density (J_{sc}) and (**d**) power conversion efficiency (PCE) values of the single-junction WBG pero-SCs treated with different concentrations of TDB from 15 devices for each condition.

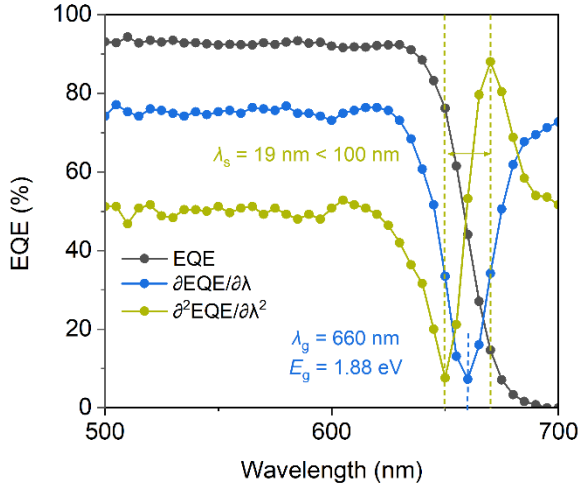

Supplementary Figure 14. The external quantum efficiency (EQE), ∂EQE/∂λ and ∂^2EQE/∂λ^2 curves of WBG pero-SCs. The EQE curve and its derivation curve of the WBG pero-SCs were used for the determination of bandgap.

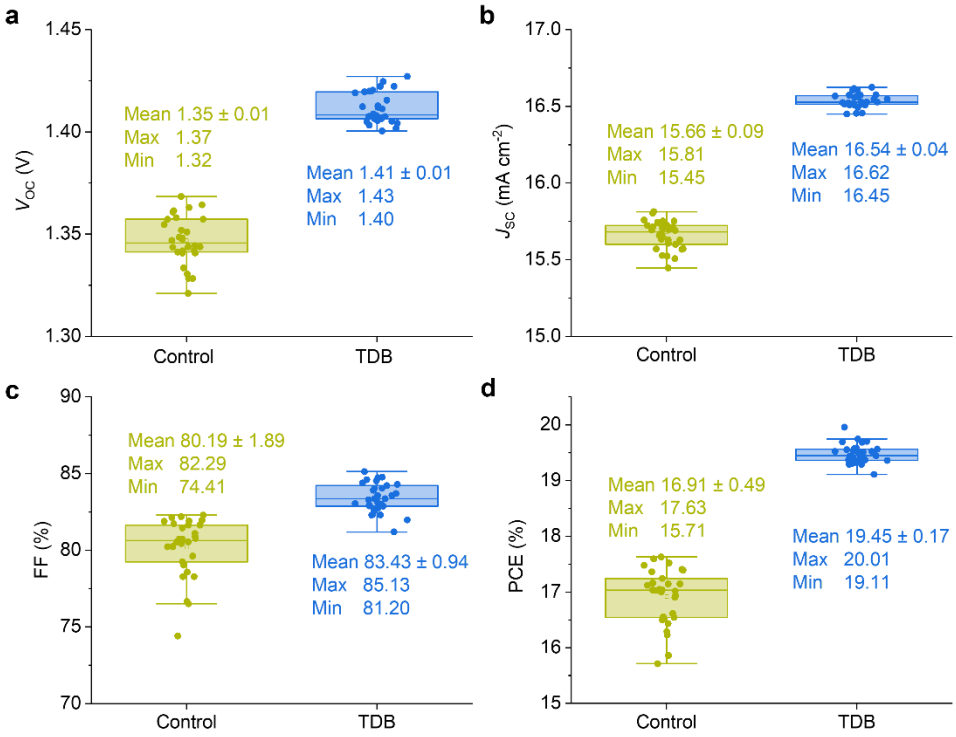

Supplementary Figure 15. Distributions of the V_{oc}, J_{sc}, FF and PCE of the control and TDB-treated single-junction WBG pero-SCs from 30 devices for each condition.

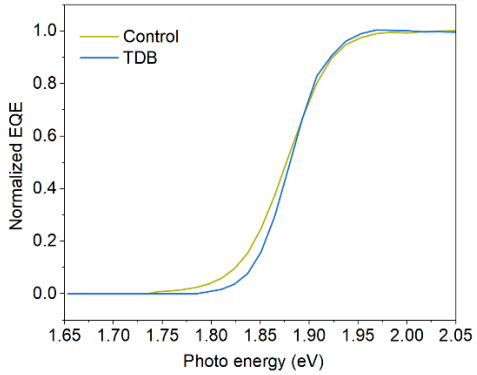

Supplementary Figure 16. Normalized EQE spectra for the control and TDB-treated WBG pero-SCs. The normalized EQE spectra of control device exhibit more pronounced sub-bandgap tail than TDB-treated device, indicating the band tail states and defect-assisted absorption below the optical bandgap.

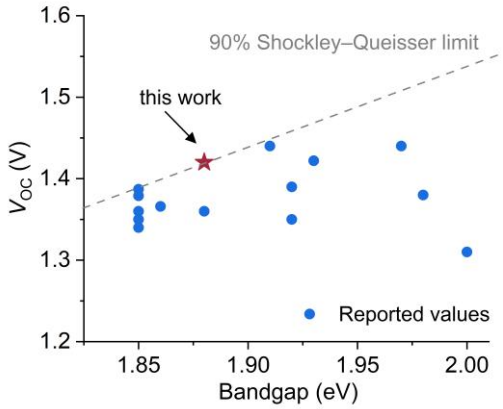

Supplementary Figure 17. Comparison of the V_{oc} between this work and other reported *p-i-n* structure WBG pero-SCs with a bandgap surpassing 1.85 eV (see Supplementary Table 2 for the reported data).

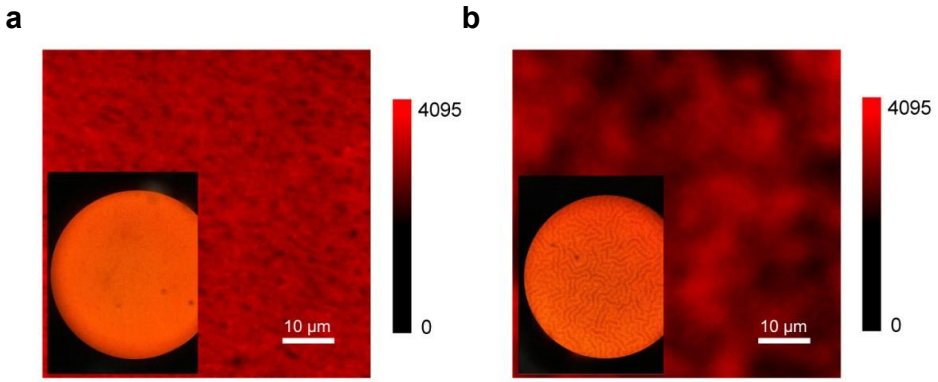

Supplementary Figure 18. Confocal photoluminescence mapping images of the TDB-treated film (**a**) and control film (**b**). The insets show optical microscopy images acquired using a 50× objective lens.

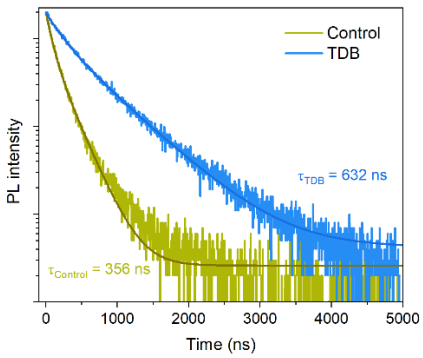

Supplementary Figure 19. Time-resolved photoluminescence of the control and TDB-treated perovskite films.

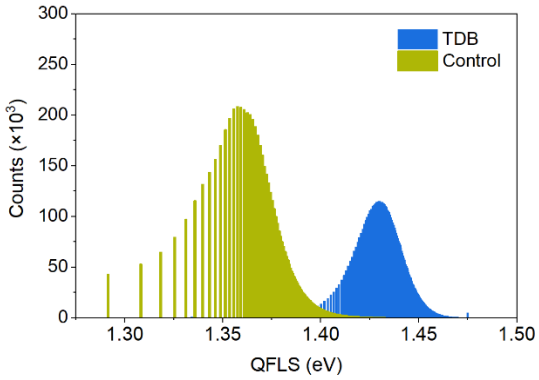

Supplementary Figure 20. Histogram of QFLS values obtained from the control and TDB-treated device stacks. Compared with the control device stack, the TDB-treated device stack shows a narrower distribution of QFLS values.

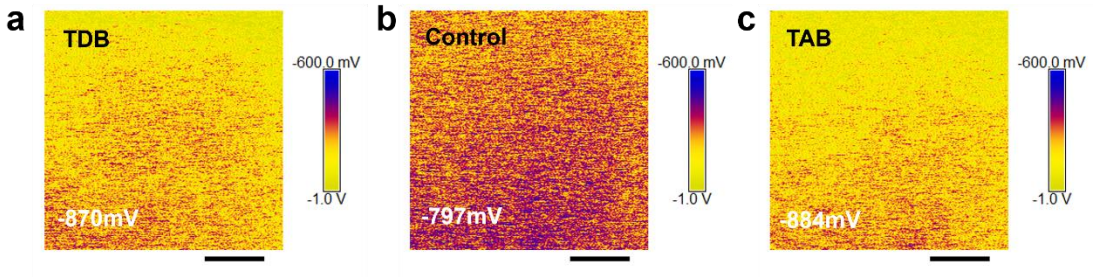

Supplementary Figure 21. Kelvin probe force microscopy (KPFM) surface-potential maps of the top surfaces of (**a**) TDB-treated, (**b**) control and (**c**) TAB-treated perovskite films. The TDB- and TAB-treated films were prepared from perovskite precursor solutions containing TDB or TAB, respectively. Scale bars, 20 μm.

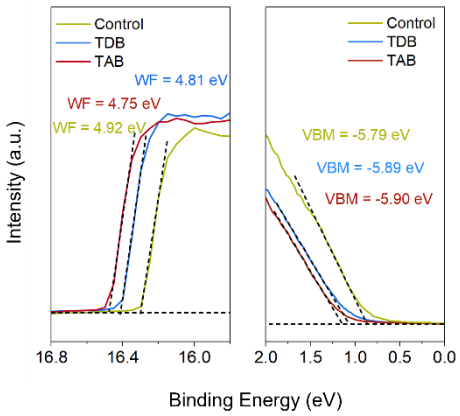

Supplementary Figure 22. Ultraviolet photoelectron spectroscopy (UPS) spectra of the top surfaces of untreated, TDB-treated, and TAB-treated perovskite films.

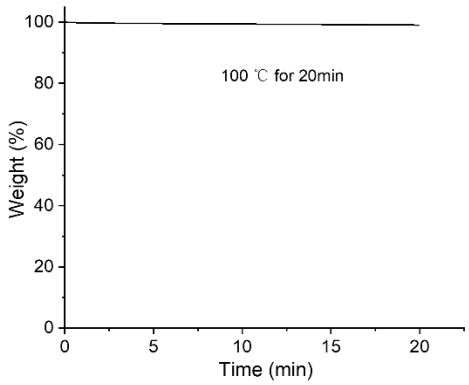

Supplementary Figure 23. Thermogravimetric analysis (TGA) curve of TDB. TDB powder was held at 100 °C for 20 min and exhibited negligible weight loss, indicating that no obvious thermally induced decomposition or transformation occurred under the annealing conditions used for perovskite film fabrication (100 °C for 15 min).

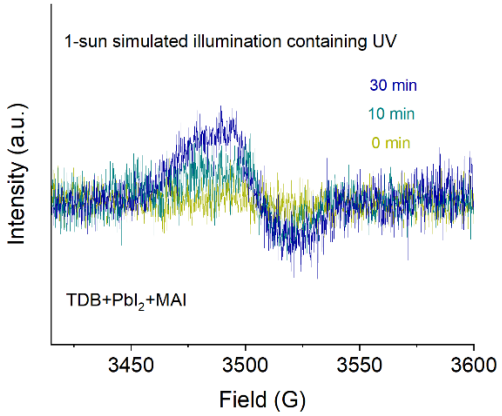

Supplementary Figure 24. Electron paramagnetic resonance (EPR) spectra of TDB under 1-sun simulated illumination containing ultraviolet components for 0, 10, and 30 min. The sample was prepared by loading a mixed powder of PbI_2, MAI and TDB into an EPR tube in a nitrogen-filled glovebox, followed by sealing the tube. The sample was frozen in liquid nitrogen prior to measurement. The electronic effect of the para-substituent plays a role in regulating the photochemical properties of trifluoromethyl aryl diazirines.[3] Electron-withdrawing para-substituents on trifluoromethyl aryl diazirines preferentially promote the formation of triplet carbenes, which are highly reactive toward molecular oxygen. In this work, the para-positioned ammoniomethyl group in TDB, owing to its electron-withdrawing character, favors the formation of a triplet carbene intermediate upon light activation, which is consistent with the EPR results. Consequently, the photogenerated triplet carbene can be rapidly captured by oxygen. In contrast, electron-donating para-substituent promotes the formation of singlet carbenes, thereby suppressing oxygen quenching and favoring C–H insertion under ambient conditions.

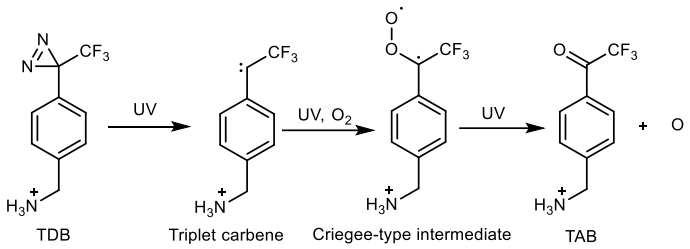

Supplementary Figure 25. Proposed photoinduced transformation pathway of TDB under illumination with ultraviolet components. Upon UV-containing irradiation, TDB undergoes photolysis of the diazirine moiety with extrusion of nitrogen, generating a triplet carbene intermediate. Then the triplet carbene is readily trapped by O_2 to generate the corresponding carbonyl oxide, namely a Criegee-type intermediate. This photolabile intermediate subsequently splits off an oxygen atom upon further irradiation, affording the ketone product TAB.[4]

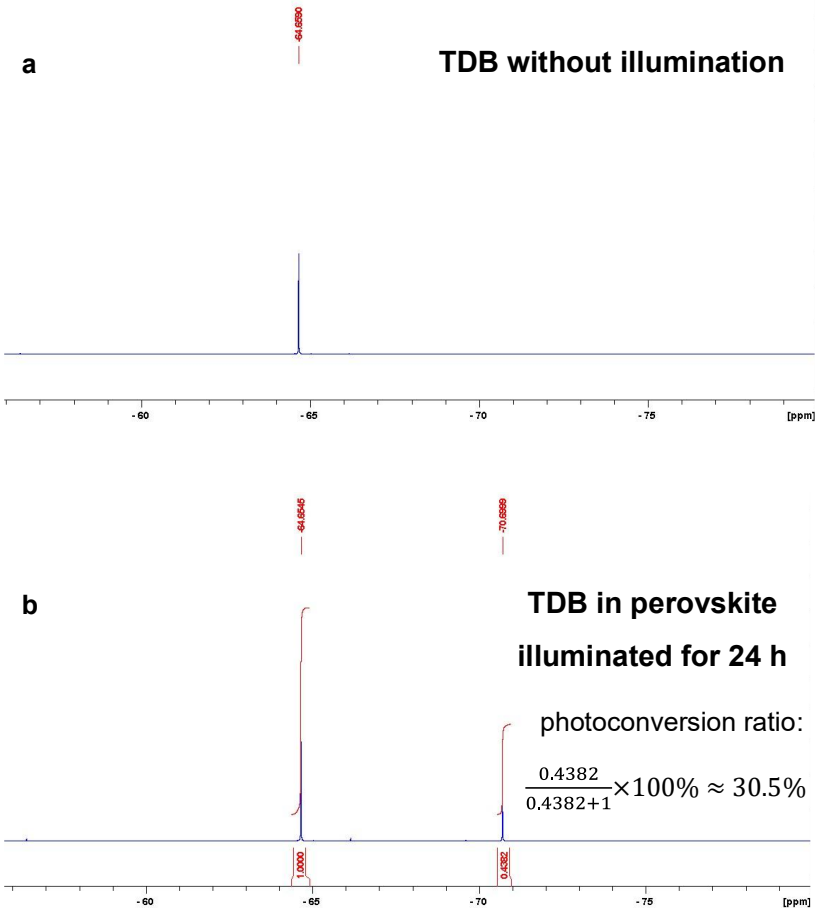

Supplementary Figure 26. Monitoring the photoconversion of TDB to TAB in perovskite films by ^{19}F NMR. To monitor the reaction and quantify the amount of TAB formed, a 1.8 M $MAPbI_3$ precursor solution containing 5 mol% TDB was prepared. Perovskite films were then deposited on 2.5 × 2.5 cm^2 FTO substrates, yielding a total of 60 films. These films were illuminated under the solar simulator containing ultraviolet components for 24 h in ambient air. After illumination, the perovskite films were scraped from the FTO substrates, yielding ~90 mg. The collected powders were dissolved in deuterated DMSO-d_6 for ^{19}F NMR characterization. The signals at −64.7 and −70.7 ppm are assigned to TDB and TAB[5], respectively. The TDB-to-TAB photoconversion ratio was estimated to be approximately 30.5% from the integrated peak areas of the two signals. A new weak signal at −66.6 ppm was assigned to the TDB dimerization product, another weak signal at −56.5 ppm was assigned to the light-induced diazoalkane intermediate[5].

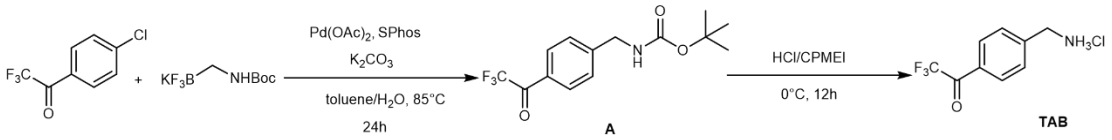

Supplementary Figure 27. Synthesis route of TAB. Because TAB was difficult to isolate from the products generated upon illumination of TDB, we independently synthesized TAB via a Suzuki coupling reaction[6] for subsequent characterization and analysis.

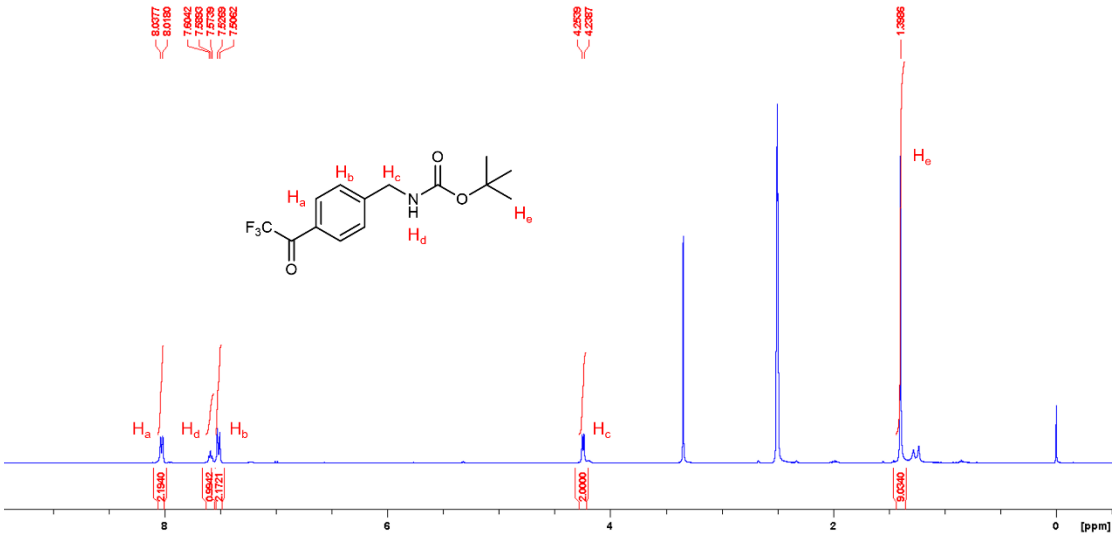

Supplementary Figure 28. ^{1}H NMR spectrum of the as-synthesized compound **A**. ^{1}H NMR (400 MHz, DMSO-d_6, δ/ppm): 8.03 (d, J = 8.1 Hz, 2H), 7.59 (t, J = 6.2 Hz, 1H), 7.52 (d, J = 8.1 Hz, 2H), 4.25 (d, J = 6.2 Hz, 2H), 1.40 (s, 9H).

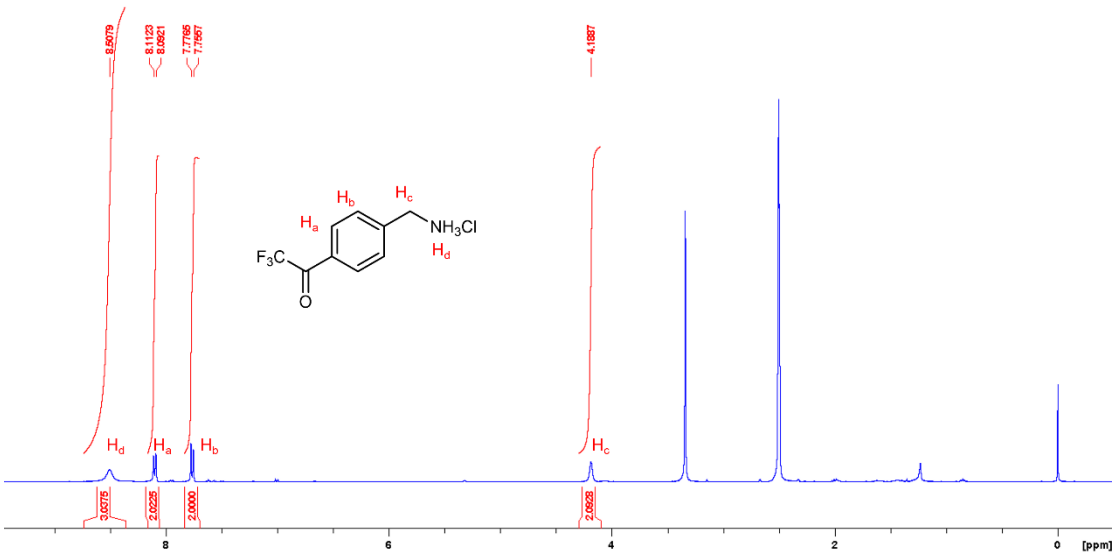

Supplementary Figure 29. ^{1}H NMR spectrum of the as-synthesized TAB. ^{1}H NMR (400 MHz, DMSO-d_6, δ/ppm): 8.51 (s, 3H), 8.10 (d, J = 8.1 Hz, 2H), 7.77 (d, J = 8.1 Hz, 2H), 4.19 (s, 2H).

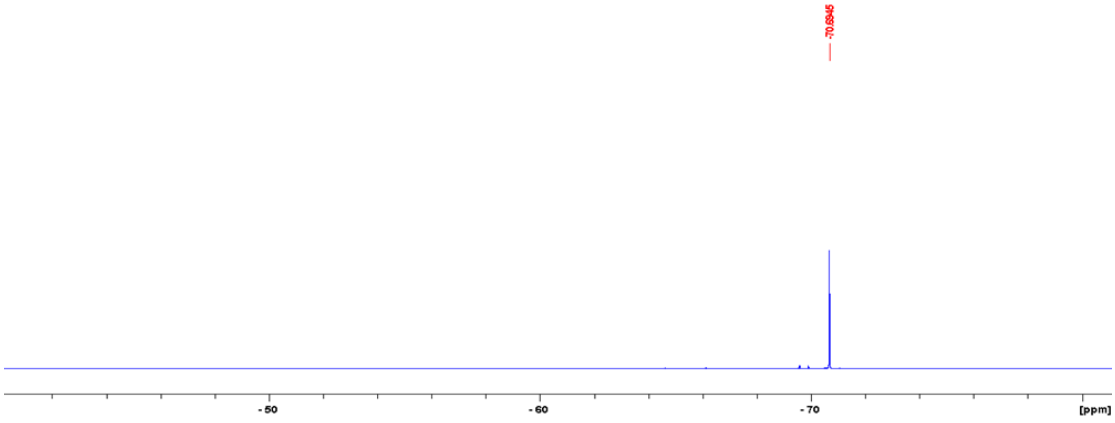

Supplementary Figure 30. ^{19}F NMR spectrum of the as-synthesized TAB. ^{19}F NMR (600 MHz, DMSO-d_6, δ/ppm): –70.7.

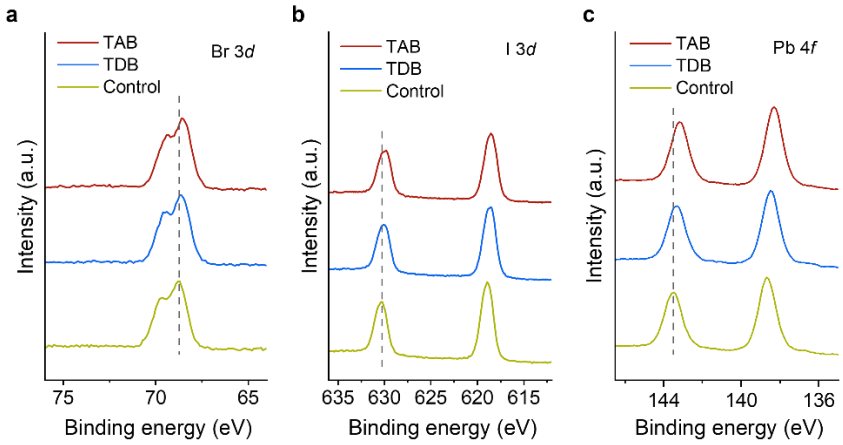

Supplementary Figure 31. X-ray photoelectron spectroscopy (XPS) spectra of the control, TDB-treated and TAB-treated perovskite films prepared from perovskite precursor solutions containing TDB or TAB as additives. (**a**) Br 3*d* spectra. (**b**) I 3*d* spectra. (**c**) Pb 4*f* spectra.

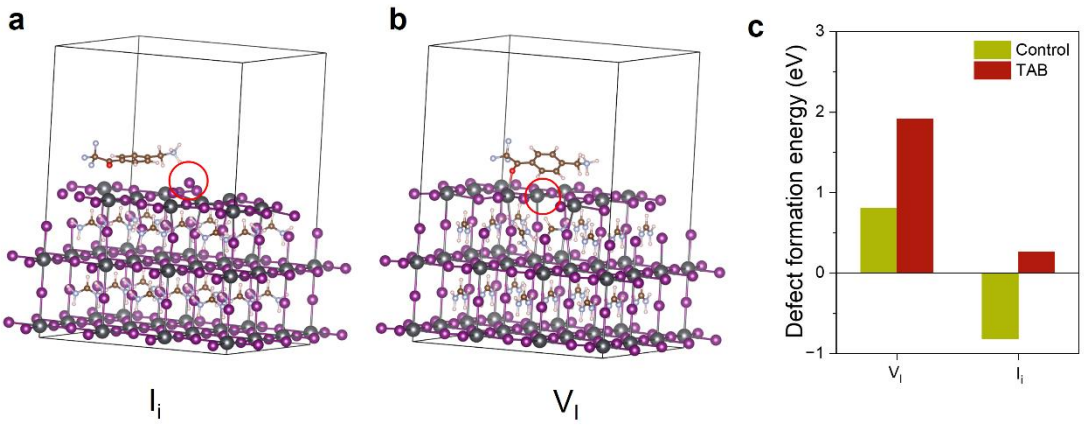

Supplementary Figure 32. Optimized structures of TAB adsorbed on the perovskite surface with (**a**) iodide interstitial (I_i) and (**b**) iodide vacancy (V_I), respectively. (**c**) Calculated formation energies of V_I and I_i of the control and TAB-treated perovskites (data are shown in Supplementary Table 5).

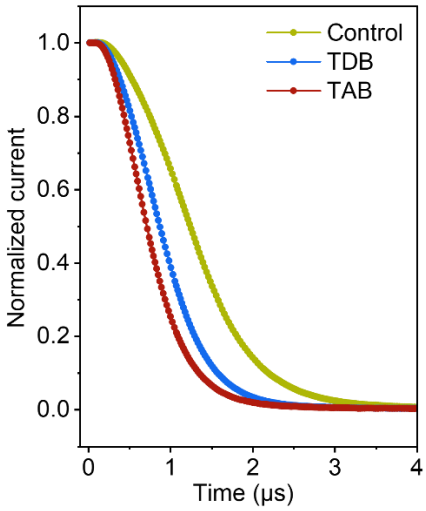

Supplementary Figure 33. Transient photocurrent (TPC) measurements of the control, TDB-treated and TAB-treated pero-SCs, where TDB and TAB were incorporated into the perovskite precursor solution as additives. The normalized TPC decay curves were fitted with a single-exponential function, yielding characteristic decay times of approximately 1.10, 0.86, and 0.68 μs, respectively.

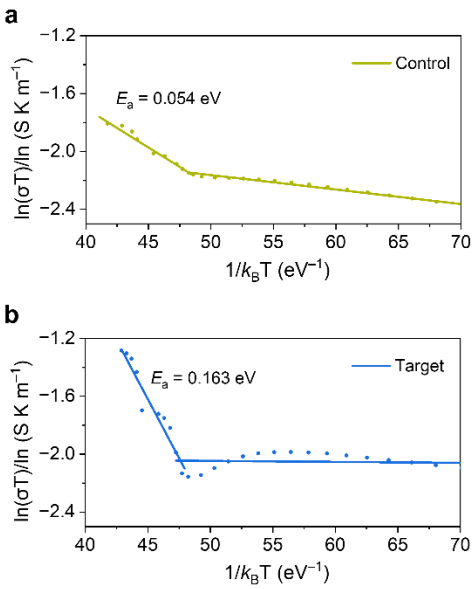

Supplementary Figure 34. Temperature-dependent electrical conductivity measurements of the control and TDB-treated devices. The control and TDB-treated devices were subjected to 24 h of light ageing before the measurements to simulate their operation under illumination after device fabrication. We derived E_a values of 0.054 eV and 0.163 eV for the control and target WBG perovskite device, respectively, based on the Arrhenius plot.

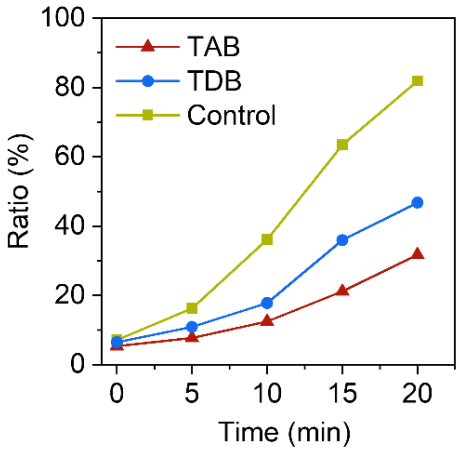

Supplementary Figure 35. Evolution of the ratio of I-rich peaks (740 nm) and intrinsic emission peak (660 nm) for the TAB-treated, TDB-treated and control perovskite films.

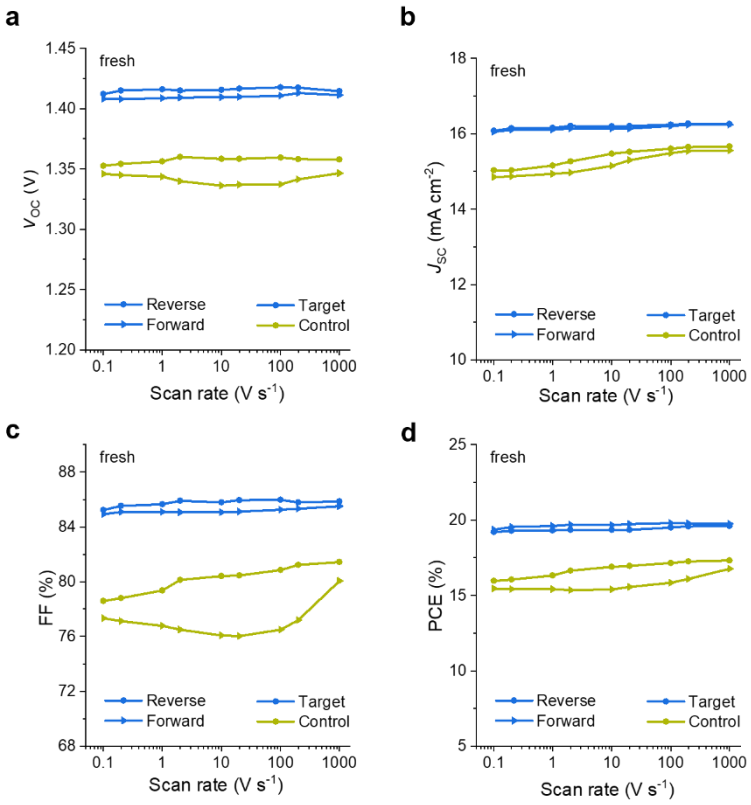

Supplementary Figure 36. V_{oc}, J_{sc}, FF and PCE of fresh target and control WBG perovskite solar cells, measured at a scan rate ranging from 0.1 V s^{-1} to 1,000 V s^{-1} in reverse and forward sweep directions. The control devices showed a pronounced reduction in J_{sc} at low scan rates. This result suggests that, before light-soaking ageing, the control devices already show pronounced ionic effects, likely associated with the high population of mobile ions due to the severe initial halide mixing inhomogeneity[7,8].

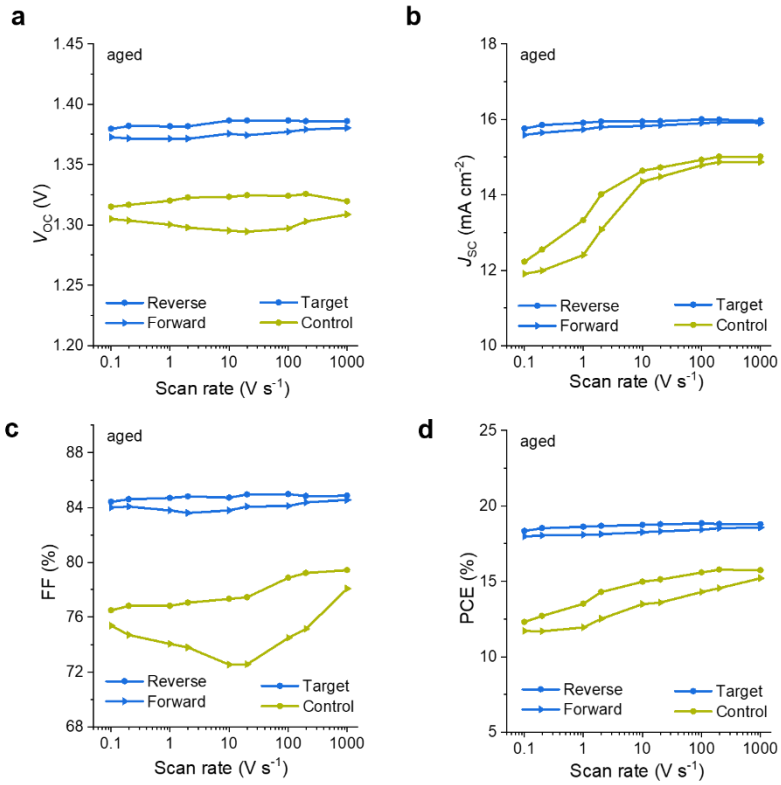

Supplementary Figure 37. V_{oc}, J_{sc}, FF and PCE of aged control and target WBG perovskite solar cells after 12 h of 1-sun light soaking, measured at a scan rate ranging from 0.1 V s^{-1} to 1,000 V s^{-1} in reverse and forward sweep directions. The J_{sc} of the aged control devices showed a stronger scan-rate dependence than that of the fresh devices, indicating more pronounced phase segregation during illumination and consequently greater ionic losses in the control devices[7,8].

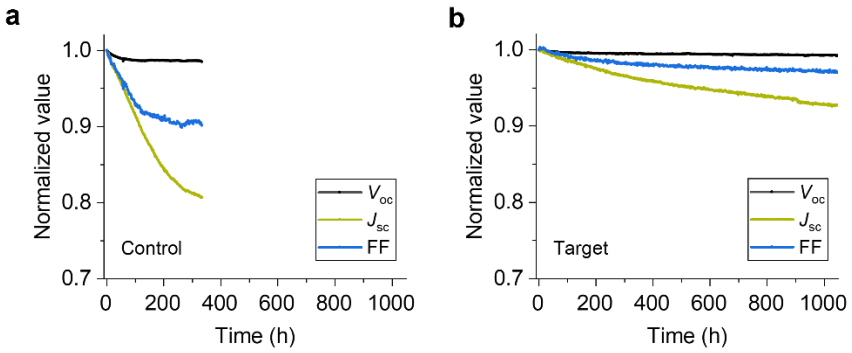

Supplementary Figure 38. The relative loss trends of V_{oc}, J_{sc}, and FF during MPP tracking testing for the control and target WBG pero-SCs. In both groups, the decrease in J_{sc} was the most pronounced among the three parameters. This result indicates that ion-induced electric-field screening, driven by ion migration under illumination, makes the largest contribution to the overall performance degradation[7].

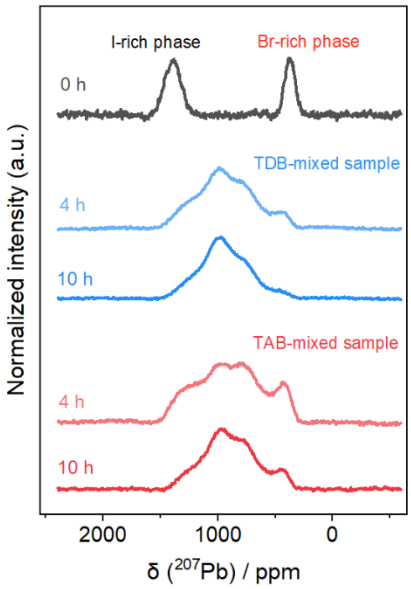

Supplementary Figure 39. ^{207}Pb solid-state NMR spectra of perovskite powders with TDB and with TAB after thermal treatment for different durations. The initial spectra at 0 h show distinct signals assigned to the iodide-rich and bromide-rich phases. Upon thermal treatment, the spectra gradually evolve toward the intermediate chemical-shift region, indicating progressive halide mixing and the formation of mixed-halide coordination environments around Pb. The comparison shows that TAB is much less effective than TDB in promoting halide mixing during thermal treatment, suggesting that TDB more effectively facilitates halide ion transport and thus accelerates halide mixing[9,10].

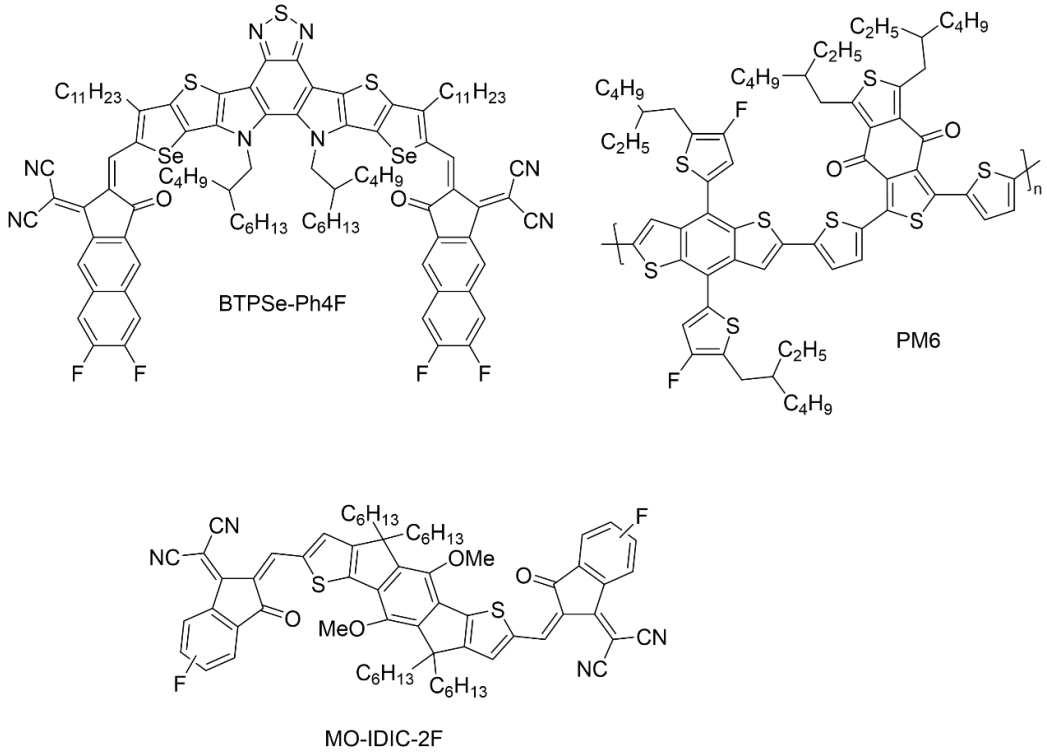

Supplementary Figure 40. Chemical structures of the polymer donor PM6, the A-DA'D-A-type acceptor material BTPSe-Ph4F and the third component MO-IDIC-2F used in the organic photovoltaic layer.

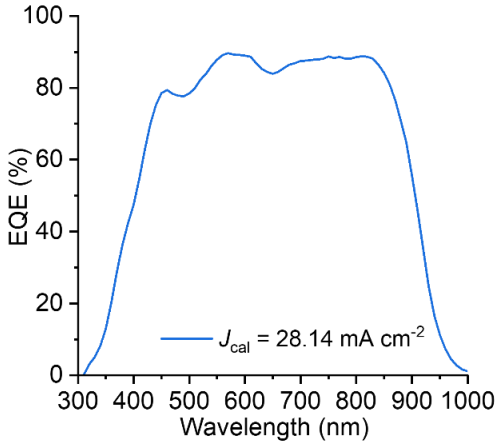

Supplementary Figure 41. EQE curve and integrated J_{cal} value of the single-junction OSC based on PM6:BTPSe-Ph4F:MO-IDIC-2F.

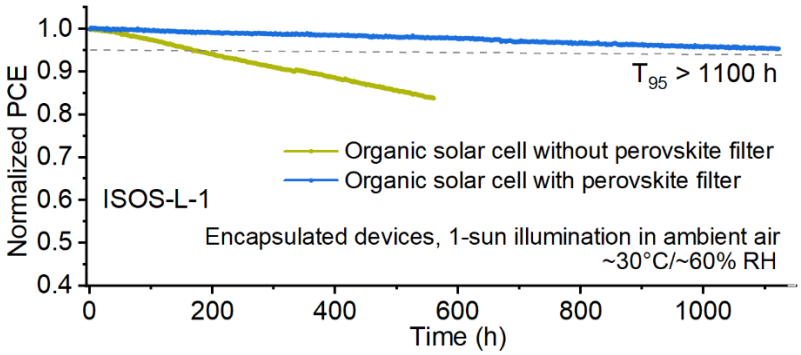

Supplementary Figure 42. Long-term MPP tracking of the encapsulated OSC without and with a WBG perovskite filter under simulated 1-sun illumination in ambient air, without temperature control (~30 °C). The WBG perovskite front cell can filter ultraviolet light and a fraction of the visible spectrum, thereby shielding the NBG organic rear cell from high-energy-photon-induced degradation, which is among the most detrimental stress factors for OSCs[11,12]. We placed quartz substrates coated with WBG perovskite films (encapsulated) in front of encapsulated OSCs in ambient air, simulating the spectral filtering scenario in the TSCs. Under continuous MPP tracking, the filtered organic device maintained over 95% of its initial output power for over 1100 h (T_{95} > 1100 h). In contrast, the OSCs without WBG perovskite filtering degraded to 84% of their initial efficiency after 550 h.

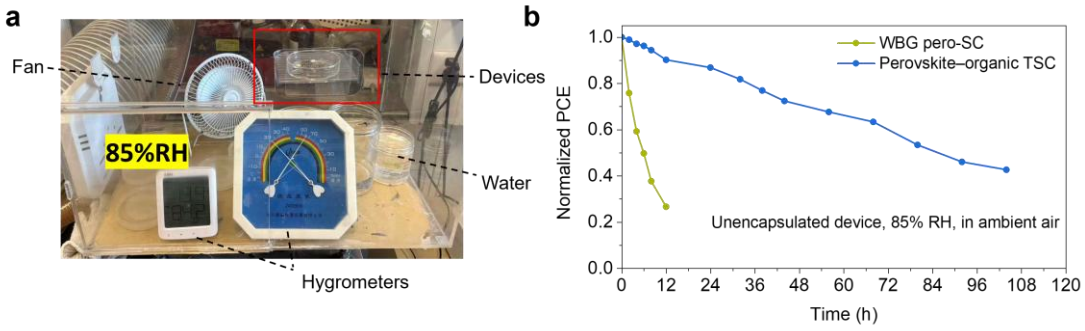

Supplementary Figure 43. a, Photograph of the humidity-controlled setup. There are devices, water, hygrometers and fan in the storage box. **b**, Operational stability of unencapsulated WBG pero-SCs and unencapsulated perovskite–organic TSCs under high-humidity accelerated ageing condition (85% relative humidity (RH) in ambient air). We investigated the operational stability advantage of perovskite–organic TSCs under high-humidity conditions due to the hydrophobic properties of the organic rear cell. The ~120 nm-thick organic active layer acts as an additional barrier shielding the perovskite front cell from moisture—a detrimental stress factor that can trigger perovskite decomposition[13]. We conducted accelerated ageing tests under 85% RH in ambient air. When comparing unencapsulated WBG perovskite single-junction devices with unencapsulated perovskite–organic TSCs, the WBG perovskite single-junction devices exhibited a rapid performance decline within the first 12 h. In contrast, the unencapsulated perovskite–organic TSCs showed markedly improved storage stability under the same high-humidity conditions.

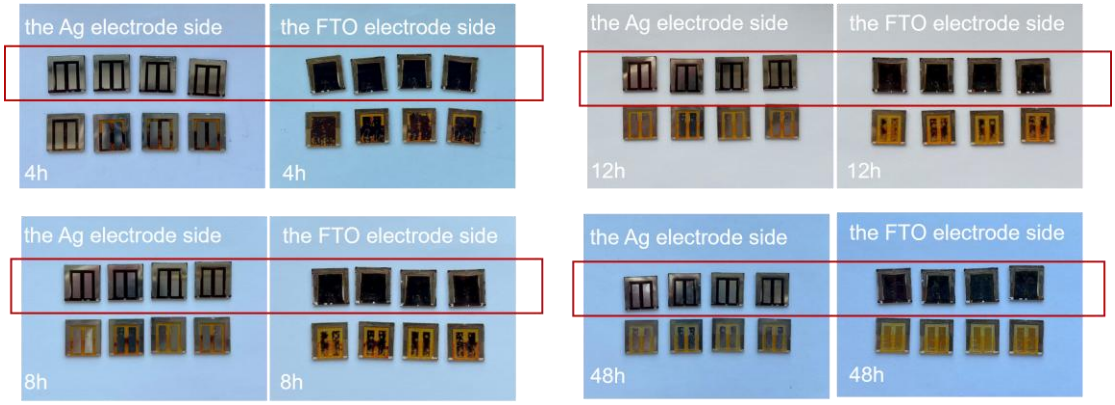

Supplementary Figure 44. Photograph of devices under high-humidity accelerated ageing condition (85% RH in ambient air). The perovskite–organic TSCs are enclosed in the red box in the photograph, with the WBG pero-SCs located below. Within only 12 h, the perovskite absorber visibly transformed from the black perovskite phase to yellow PbI_2 under the high-humidity conditions. Concurrently, the Ag electrode exhibited obvious degradation. In contrast, the perovskite absorber in the unencapsulated perovskite–organic TSCs retained its black phase under the same high-humidity conditions.

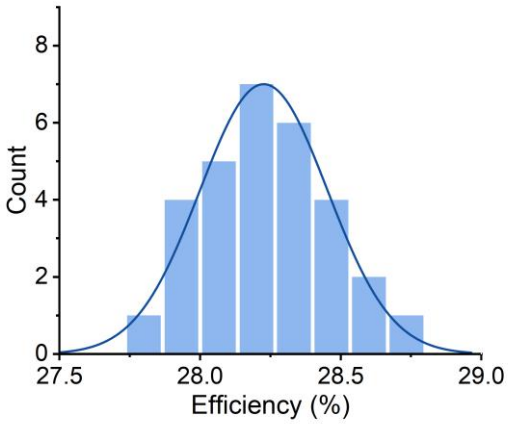

Supplementary Figure 45. Distribution of the PCEs of the perovskite–organic TSCs based on 30 devices.

Supplementary Figure 46. The certificate of our representative perovskite–organic TSC with steady-state PCE of 28.04% from the National Photovoltaic Industry Measurement and Test Center (NPVM). The certified PCE from reverse and forward scans are 28.23% and 27.73%, respectively. The certificate also includes the measurement of relative spectral responsivity for the measured device, which is used to calculate the spectral mismatch factor and thus correct the simulator's nonideal spectral irradiance distribution.

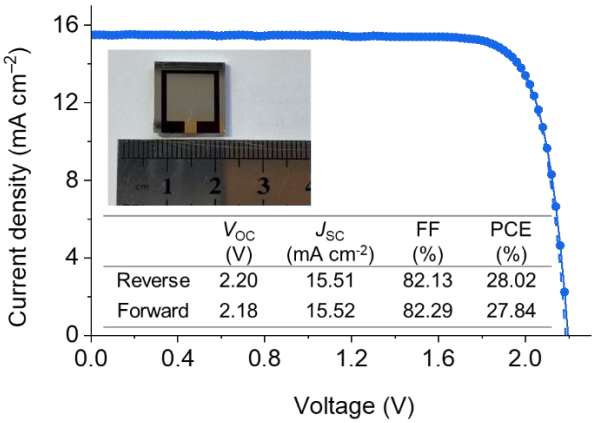

Supplementary Figure 47. *J*–*V* curve and photograph of the representative 1-cm^2 perovskite–organic TSC.

Supplementary Tables

Supplementary Table 1. Calculated binding energies (eV) between different molecules and I^-/Br^- ions.

Species	I^-	Br^-
DMF	−0.5309	−0.6504
DMSO	−0.6780	−0.8193
TDB	−4.7525	−5.1680
TAB	−4.8602	−5.2180

Supplementary Table 2. Summary of photovoltaic performance of the *p-i-n* structure WBG pero-SCs with E_g over 1.85 eV from reported literature.

E_g (eV)	V_{oc} (V)	J_{sc} (mA cm^{-2})	FF (%)	PCE (%)	V_{oc} × FF (V)	Reference
1.85	1.34	15.6	81.0	16.8	1.085	12
1.85	1.360	16.21	83.21	18.14	1.132	14
1.85	1.350	16.78	83.29	18.87	1.124	15
1.86	1.366	16.10	84.20	18.52	1.150	16
1.88	1.36	16.1	83.8	18.4	1.140	17
1.91	1.44	14.38	81.2	16.87	1.169	18
1.92	1.39	14.3	83.5	16.2	1.161	19
1.92	1.35	15.1	83.7	17.0	1.130	20
1.97	1.44	12.8	83	15.3	1.195	21
1.93	1.422	14.18	83.79	16.90	1.191	22
2.00	1.31	13.5	75.9	13.4	0.994	23
1.85	1.387	16.06	84.20	18.76	1.168	24
1.98	1.38	14.0	77.8	14.8	1.074	25
1.85	1.379	16.72	80.90	18.65	1.116	26
1.88	1.42	16.55	85.13	20.01	1.209	This work

Supplementary Table 3. TRPL parameters by dual exponential fitting.

Perovskite	A_1	τ_1 (ns)	A_2	τ_2 (ns)	τ (ns)
Control	820	176	430	418	310
TDB	861	313	585	721	562

Supplementary Table 4. The maximum and minimum points (φ_{max} and φ_{min}) of the electrostatic potential and adsorption energy of TAB and TDB.

molecule	φ_{max} (kcal/mol)	φ_{min}(kcal/mol)	adsorption energies (eV)
TAB	158.1	31.1	–8.2
TDB	154.8	33.4	–6.9

Supplementary Table 5. Calculated formation energies (eV) of V_I and I_i of the control and TAB-treated perovskites.

Sample	V_I	I_i
Control	0.81	−0.82
TAB	1.92	0.27

Supplementary Table 6. Device parameters of the WBG pero-SCs with different active-layer thicknesses without TDB treatment under AM 1.5G illumination at 100 mW cm^{-2}.

Perovskite active layer thickness		V_{oc} (V)	J_{sc} (mA cm^{-2})	FF (%)	PCE (%)
	Mean	1.36 ± 0.005	15.5 ± 0.06	83.2 ± 0.44	17.5 ± 0.17
350 nm	Max	1.37	15.5	83.8	17.8
	Min	1.35	15.4	82.6	17.3
	Mean	1.36 ± 0.006	15.6 ± 0.09	82.1 ± 0.56	17.5 ± 0.17
500 nm	Max	1.37	15.7	82.8	17.7
	Min	1.35	15.4	80.8	17.1
	Mean	1.36 ± 0.006	15.7 ± 0.10	81.1 ± 0.57	17.3 ± 0.23
650 nm	Max	1.36	15.9	82.2	17.6
	Min	1.34	15.6	80.4	16.9
	Mean	1.35 ± 0.008	15.9 ± 0.11	80.6 ± 0.86	17.3 ± 0.29
800 nm	Max	1.36	16.0	82.0	17.8
	Min	1.34	15.7	79.0	16.9

Notes: While the J_{sc} increases with increasing film thickness, both the V_{oc} and FF exhibit a gradual decline, which can be attributed to the accelerated crystallization kinetics induced by the higher-concentration precursor solution. The average values and the deviations are calculated from 15 independent devices.

Supplementary Table 7. Device parameters of the WBG pero-SCs with different active-layer thicknesses with TDB treatment under AM 1.5G illumination at 100 mW cm^{-2}.

Perovskite active layer thickness		V_{oc} (V)	J_{sc} (mA cm^{-2})	FF (%)	PCE (%)
	Mean	1.41 ± 0.004	16.2 ± 0.04	84.4 ± 0.54	19.3 ± 0.15
350 nm	Max	1.41	16.3	84.9	19.5
	Min	1.40	16.1	83.3	19.0
	Mean	1.40 ± 0.004	16.4 ± 0.06	84.2 ± 0.50	19.4 ± 0.06
500 nm	Max	1.41	16.5	84.8	19.6
	Min	1.40	16.3	83.5	19.2
	Mean	1.41 ± 0.007	16.6 ± 0.07	84.2 ± 0.63	19.6 ± 0.22
650 nm	Max	1.42	16.7	85.1	20.0
	Min	1.40	16.4	83.2	19.3
	Mean	1.40 ± 0.007	16.7 ± 0.07	83.7 ± 0.50	19.6 ± 0.15
800 nm	Max	1.40	16.9	84.7	19.9
	Min	1.38	16.7	83.2	19.4

Notes: The introduction of TDB enables WBG perovskites to maintain high V_{oc} and FF under high precursor concentrations. The average values and the deviations are calculated from 15 independent devices.

Supplementary Table 8. Device parameters of the perovskite–organic TSCs with different TDB-treated perovskite active-layer thicknesses under AM 1.5G illumination at 100 mW cm^{-2}.

Perovskite active layer thickness		V_{oc} (V)	J_{sc} (mA cm^{-2})	FF (%)	PCE (%)
	Mean	2.18 ± 0.006	15.3 ± 0.05	82.7 ± 0.32	27.7 ± 0.12
500 nm	Max	2.20	15.4	83.1	27.9
	Min	2.17	15.3	82.1	27.5
	Mean	2.19 ± 0.008	15.5 ± 0.05	83.2 ± 0.48	28.3 ± 0.23
650 nm	Max	2.20	15.6	83.9	28.8
	Min	2.18	15.4	82.5	28.0
	Mean	2.17 ± 0.006	15.4 ± 0.03	82.9 ± 0.55	27.7 ± 0.22
800 nm	Max	2.18	15.4	83.7	28.0
	Min	2.16	15.3	82.1	27.4

Notes: The average values and the deviations are calculated from 15 independent devices.

Supplementary Table 9. Summary of the reported, independently certified perovskite–organic tandem solar cells.

Year	V_{oc} (V)	J_{sc} (mA cm^{-2})	FF (%)	PCE (%)	Certified PCE (%)	Reference
2022	2.060	14.83	77.20	23.60	22.95	27
2022	2.150	14.00	80.00	24.00	23.10	12
2024	2.151	14.36	81.65	25.22	24.27	28
2024	2.120	14.68	82.97	25.82	25.06	29
2024	2.144	14.65	80.02	25.13	23.40	16
2024	2.126	14.38	83.62	25.56	24.65	19
2024	2.160	15.40	79.40	26.40	25.70	17
2025	2.21	14.51	80.77	25.90	25.08	30
2025	2.148	14.60	83.38	26.15	25.34	31
2025	2.21	14.42	81.75	26.05	24.53	32
2025	2.14	15.15	82.4	26.7	26.4	33
2025	2.120	15.21	82.08	26.46	25.82	34
2025	2.20	15.64	83.69	28.80	28.04 (steady-state)	This work

Supplementary References

1. Jung, M., Ji, S.-G., Kim, G. & Seok, S. I. Perovskite precursor solution chemistry: from fundamentals to photovoltaic applications. *Chem. Soc. Rev.* **48**, 2011–2038 (2019).
2. Abraham, R. J., Canton, M. & Griffiths, L. Proton chemical shifts in NMR: part 17. Chemical shifts in alkenes and anisotropic and steric effects of the double bond. *Magn. Reson. Chem.* **39**, 421–431 (2001).
3. Musolino, S. F., Pei, Z., Bi, L., DiLabio, G. A. & Wulff, J. E. Structure–function relationships in aryl diazirines reveal optimal design features to maximize C–H insertion. *Chem. Sci.* **12**, 12138–12148 (2021).
4. Sander, W. W. Effects of electron-withdrawing groups on carbonyl *O*-oxides. Trifluoroacetophenone *O*-oxide and hexafluoroacetone *O*-oxide. *J. Org. Chem.* **53**, 121–126 (1988).
5. Lepage, M. L. & Gras, E. The versatility of diazirines: properties, synthetic and modern applications. *Chem. Eur. J.* **31**, e202500414 (2025).
6. Molander, G. A. & Shin, I. Synthesis and Suzuki–Miyaura cross-coupling reactions of potassium Boc-protected aminomethyltrifluoroborate with aryl and hetaryl halides. *Org. Lett.* **13**, 3956–3959 (2011).
7. Thiesbrummel, J. et al. Ion-induced field screening as a dominant factor in perovskite solar cell operational stability. *Nat. Energy* **9**, 664–676 (2024).
8. Balaguera, E. H. et al. 'Ion-freeze' efficiency in perovskite solar cells: time scales for ion immobilization. *EES Sol.* **1**, 1051–1060 (2025).
9. Maschwitz, T. et al. How crystallization additives govern halide perovskite grain growth. *Nat. Commun.* **16**, 9894 (2025).
10. Greve, C. et al. To stop or to shuttle halides? The role of an ionic liquid in thermal halide mixing of hybrid perovskites. *ACS Energy Lett.* **8**, 5041–5049 (2023).
11. Wu, X. et al. Improved stability and efficiency of perovskite/organic tandem solar cells with an all-inorganic perovskite layer. *J. Mater. Chem. A* **9**, 19778–19787 (2021).
12. Brinkmann, K. O. et al. Perovskite–organic tandem solar cells with indium oxide interconnect. *Nature* **604**, 280–286 (2022).
13. Ma, Y. et al. Crystallization-activated moisture barrier for high-tolerance manufacturing of perovskite solar cells. *Sci. Adv.* **11**, eady5703 (2025).
14. An, Y. et al. Optimizing crystallization in wide-bandgap mixed halide perovskites for high-efficiency solar cells. *Adv. Mater.* **36**, 2306568 (2024).
15. Wang, X. et al. Highly efficient perovskite/organic tandem solar cells enabled by mixed-cation surface modulation. *Adv. Mater.* **35**, 2305946 (2023).
16. Guo, X. et al. Stabilizing efficient wide-bandgap perovskite in perovskite-organic tandem solar cells. *Joule* **8**, 2554–2569 (2024).
17. Jiang, X. et al. Isomeric diammonium passivation for perovskite–organic tandem solar cells. *Nature* **635**, 860–866 (2024).
18. Guo, Y. et al. A universal surface fixed charge reconstruction strategy to minimize contact loss in wide bandgap perovskite photovoltaics. *Energy Environ. Sci*. **18**, 4916–4924 (2025).

19. Wu, X. et al. Optimization of charge extraction and interconnecting layers for highly efficient perovskite/organic tandem solar cells with high fill factor. *Adv. Mater.* **36**, 2410692 (2024).
20. Sun, S. et al. All-inorganic perovskite-based monolithic perovskite/organic tandem solar cells with 23.21% efficiency by dual-interface engineering. *Adv. Energy Mater.* **13**, 2204347 (2023).
21. Wang, J. et al. Halide homogenization for low energy loss in 2-eV-bandgap perovskites and increased efficiency in all-perovskite triple-junction solar cells. *Nat. Energy* **9**, 70–80 (2024).
22. Liu, S. et al. Triple-junction solar cells with cyanate in ultrawide-bandgap perovskites. *Nature* **628**, 306–312 (2024).
23. Wang, Z. et al. Suppressed phase segregation for triple-junction perovskite solar cells. *Nature* **618**, 74–79 (2023).
24. Song, Z. et al. Optimization of crystallization dynamics in wide-bandgap bromine–iodine perovskite films for high-performance perovskite–organic tandem solar cells. *Energy Environ. Sci.* **18**, 4883–4892 (2025).
25. Xu, F. et al. Monolithic perovskite/perovskite/silicon triple-junction solar cells with cation double displacement enabled 2.0 eV perovskites. *Joule* **8,** 224–240 (2024).
26. Xie, G. et al. Crystallization thermodynamics regulation of 1.85 eV wide-bandgap perovskite for efficient and stable perovskite-organic tandem photovoltaics. *Angew. Chem. Int. Ed.* **64,** e202501764 (2025).
27. Chen, W. et al. Monolithic perovskite/organic tandem solar cells with 23.6% efficiency enabled by reduced voltage losses and optimized interconnecting layer. *Nat. Energy* **7**, 229–237 (2022).
28. Wu, S. et al. Redox mediator-stabilized wide-bandgap perovskites for monolithic perovskite–organic tandem solar cells. *Nat. Energy* **9**, 411–421 (2024).
29. Zhang, Z. et al. Suppression of phase segregation in wide-bandgap perovskites with thiocyanate ions for perovskite/organic tandems with 25.06% efficiency. *Nat. Energy* **9**, 592–601 (2024).
30. Han, Y. et al. Inorganic perovskite/organic tandem solar cells with 25.1% certified efficiency via bottom contact modulation. *Nat. Energy* **10**, 513–525 (2025).
31. Dong, P. et al. Retarding phase segregation via lattice reinforcement for efficient and stable perovskite/organic tandem solar cells. *Angew. Chem. Int. Ed.* **64**, e202502391 (2025).
32. An, Y. et al. Balancing carrier transport in interconnection layer for efficient perovskite/organic tandem solar cells. *Nat. Commun.* **16**, 2759 (2025).
33. Jia, Z. et al. Efficient near-infrared harvesting in perovskite–organic tandem solar cells. *Nature* **643**, 104–110 (2025).
34. Wang, Y.-D. et al. Regulating wide-bandgap perovskite face-on stacking in hybrid-deposited perovskite/organic tandem solar cells. *Nat. Commun.* **16**, 6142 (2025).